optica

Far-field transient absorption nanoscopy with sub-50 nm optical super-resolution

Yali Bi,[1,3,†] Chi Yang,[1,3,†] Lei Tong,[2,†] Haozheng Li,[1,3] Boyu Yu,[1,3] Shuai Yan,[1,3] Guang Yang,[1,3] Meng Deng,[1] Yi Wang,[1] Wei Bao,[4,7] Lei Ye,[2,6] and Ping Wang[1,3,5]

[1]Britton Chance Center for Biomedical Photonics, Wuhan National Laboratory for Optoelectronics-Huazhong University of Science and Technology, Wuhan, Hubei 430074, China
[2]School of Optical and Electronic Information and Wuhan National Laboratory for Optoelectroncis, Huazhong University of Science and Technology, Wuhan, Hubei 430074, China
[3]MoE Key Laboratory for Biomedical Photonics, Collaborative Innovation Center for Biomedical Engineering, School of Engineering Sciences, Huazhong University of Science and Technology, Wuhan, Hubei 430074, China
[4]Department of Electrical and Computer Engineering, University of Nebraska-Lincoln, Lincoln, Nebraska 68588, USA
[5]e-mail: p_wang@hust.edu.cn
[6]e-mail: leiye@hust.edu.cn
[7]e-mail: wbao@unl.edu

Nanoscopic imaging or characterizing is the mainstay of the development of advanced materials. Despite great progress in electronic and atomic force microscopies, label-free and far-field characterization of materials with deep sub-wavelength spatial resolution has long been highly desired. Herein, we demonstrate far-field super-resolution transient absorption (TA) imaging of two-dimensional material with a spatial resolution of sub-50 nm. By introducing a donut-shaped blue saturation laser, we effectively suppress the TA transition driven by near-infrared (NIR) pump–probe photons, and push the NIR-TA microscopy to sub-diffraction-limited resolution. Specifically, we demonstrate that our method can image the individual nano-grains in graphene with lateral resolution down to 36 nm. Further, we perform super-resolution TA imaging of nano-wrinkles in monolayer graphene, and the measured results are very consistent with the characterization by an atomic force microscope. This direct far-field optical nanoscopy holds great promise to achieve sub-20 nm spatial resolution and a few tens of femtoseconds temporal resolution upon further improvement and represents a paradigm shift in a broad range of hard and soft nanomaterial characterization. © 2020 Optical Society of America under the terms of the OSA Open Access Publishing Agreement

https://doi.org/10.1364/OPTICA.402009

1. INTRODUCTION

Far-field optical super-resolution microscopy has been routinely adopted for biological imaging with extraordinary resolution beyond the diffraction limit [1,2]. Despite the tremendous scientific advances and successes made, the current super-resolution microscopy critically relies on various fluorescent labels and exogenous dyes, and the applications are limited mainly in fluorescent labeled cells and tissues, followed by challenges in sample preparation, label toxicity, photo-bleaching and auto-fluorescence, inevitably [1,3]. In other research fields, especially for material science, the usage of scanning electron microscopy (SEM), transmission electron microscopy (TEM), scanning tunneling microscopy (STM), atomic force microscopy (AFM), and near-field scanning optical microscopy (NSOM) [4,5] is very prominent and successful for high-resolution imaging. Nevertheless, these imaging processes typically require strict surface cleaning, time-consuming sample preparation, mostly tedious operation, and even specific environments, such as high vacuum. Although the

direct optical super-resolution imaging could be undoubtedly advantageous over traditional nanoscopies, feasible far-field optical alternatives with comparable spatial resolution remain elusive. Without labels, far-field spontaneous Raman spectroscopy may screen artifacts on materials with definitive analytical details, but the image resolution is limited well above ∼200 nm, far from ideal. To achieve better spatial resolution, pump–probe [6–8], coherent Raman scattering (CRS) [9–14], and other microscopies [15–18] have been proposed. With persistent pursuits, higher-order near-infrared (NIR) coherent anti-Stokes Raman scattering (CARS) microscopy has realized vibrational super-resolution imaging of unlabeled cells with spatial resolution ∼190 nm [19]. An extension of pump–probe microscopy based on the saturation effect [20,21] demonstrated super-resolution imaging of two-dimensional (2D) material with spatial resolution approaching ∼100 nm [22,23]. However, there is still a huge gap for far-field optical imaging and nanostructures in materials.

Here, we achieve sub-50 nm super-resolution transient absorption (TA) nanoscopy by applying a very effective saturation laser

at a visible wavelength. In previously reported saturation-based TA super-resolution modalities [22,23], the photon energy of the saturation laser was at a level similar to applied NIR excitation lasers. In our method, the wavelength of saturation photons is for the first time tuned to the visible range, by which the saturation laser can effectively clear the electronic population in the valence band of graphene and significantly suppress the efficiency of the NIR-TA process. We demonstrate super-resolution imaging of individual nano-grains on graphene with lateral resolution down to 36 nm, and the achieved spatial resolution is comparable even to near-field images [24]. By saturated TA nanoscopy (STAN), we also characterize the nano-wrinkles in monolayer graphene, which are in great consistency with the corresponding AFM image. In the future, STAN has great potential to achieve sub-20 nm spatial resolution upon further improvement and serves a broad range of nanomaterial characterizations.

2. RESULTS AND DISCUSSION

The proposed super-resolution STAN system is modified on the conventional saturated TA microscope (details in Experimental Section, Supplement 1). Figure 1(a) illustrates the principle of the STAN system. The superimposed pump, probe, and saturation lasers are focused on the graphene sample by an objective with 1.49 numerical aperture (NA). Because the TA process is induced in the very center of the focused spot, the probe laser will respond to the modulation of the pump laser. However, in the peripheral region of the focused spot, the process of TA is significantly suppressed due to the presence of the saturation donut-shaped 451 nm laser, which leads to elimination of the modulation response in the probe beam. As a result, the lock-in signal detected in the probe beam reflects only the TA signal arisen from the very center of the laser focus. Specially, the 451 nm saturation photons possess higher energy than NIR-TA photons, which results in very effective depletion of electrons in the valence band of the monolayer graphene [Fig. 1(b)]. The diagram depicting the optical transitions of STAN and other super-resolution NIR systems is shown in Fig. S1, Supplement 1. We found that the saturation laser with higher photon energy relative to that of the pump and probe lasers is the most key factor responsible for improved spatial resolution, other than the saturation intensity. As shown in Fig. S1(a), Supplement 1, the electrons in graphene can undergo interband photoexcitation from the valence band to the conduction band upon laser excitation. The photoexcited carriers further experience carrier relaxation through several intraband and interband relaxation channels. Upon excessive or saturated photon excitation, the electrons in the valence band near the Dirac point can be effectively depleted due to Pauli blocking and band filling, [25–28], and the concentrated holes and electrons near the Dirac cone will block further absorption of photons and transient transition with less energy within the band edge. Thus, the saturation photons with higher energy are the key factor to raise this saturation band edge. As a result, the adopted high-energy saturation photons in the donut-shaped ring will ensure very effective TA saturation and further enhancement of the imaging resolution. Meanwhile, the shorter wavelength applied for the saturation laser will also result in a smaller donut-shaped ring and contribute to an improvement in spatial resolution.

As shown in Fig. 1(c), a dual-output femtosecond laser system provides two phase-locked lasers for the pump beam at 1040 nm and probe beam at 902 nm. Meanwhile, the 902 nm probe beam is split to generate the saturation laser at 451 nm by a frequency
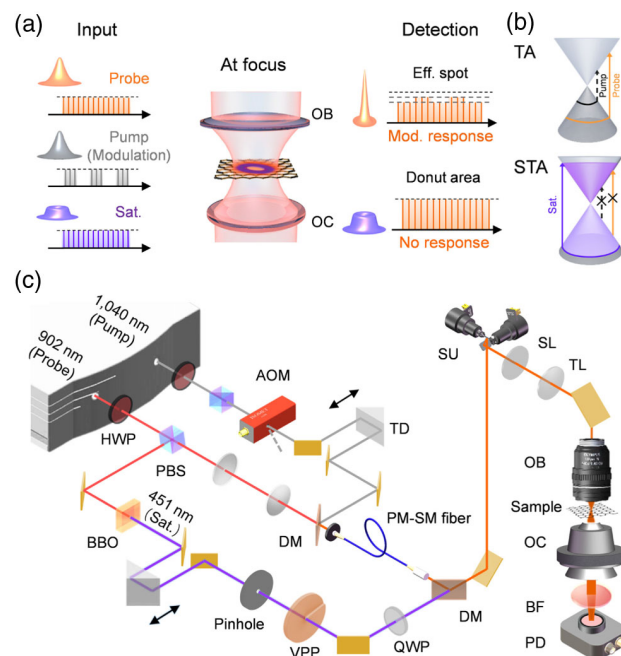

Fig. 1. Schematic of saturated transient absorption nanoscopy (STAN). (a) Principle of STAN system. Pump, probe, and donut-shaped saturation lasers are superimposed and focused on graphene sample. Due to the significant transient absorption (TA) suppression in the saturated donut-shaped region of the focus, lock-in detection of the probe laser reflects only the TA signal arisen from the very center of the laser focus. (b) Energy diagrams of TA and STA transition in graphene. (c) Real experimental schematic diagram of the STAN setup. HWP, half-wave plate; PBS, polarization beam splitter; AOM, acousto-optic modulator; TD, time delay; DM, dichroic mirror; PM-SM fiber, polarization-maintaining single-mode fiber; QWP, quarter-wave plate; VPP, vortex phase plate; SU, scanning unit; SL, scanning lens; TL, tube lens; OB, objective; OC, oil condenser; BF, band-pass filter; PD, photodiode.

doubling beta-barium borate (BBO) crystal. After spatial filtering by a 25 nm diameter pinhole, the saturation laser is engineered to donut shape with a vortex phase plate (VPP) and further collinearly combined with pump–probe lasers, which are spatially filtered by a 0.3 m long polarization-maintaining single-mode (PM-SM) fiber (Fig. S2, Supplement 1). Prior to the laser scanning by a 2D galvanometer, the pump beam is modulated in intensity for further lock-in detection, and two independent time-delay lines are adopted to match the pulse delays among pump, probe, and saturation lasers. Further, we characterize the laser scanning performance of the donut-shaped saturation laser by imaging 80 nm gold beads (Fig. S3, Supplement 1).

First, we characterized the saturation efficiency by measuring pump–probe spectra and saturation responses depending on the laser power of a Gaussian mode saturation pulse (pulse width measured in Fig. S4, Supplement 1). As shown in Fig. 2(a), we tuned the timing of the 451 nm saturation laser pulse relative to the pulse of pump–probe lasers, and measured the TA signal depression. After the 451 nm saturation laser was introduced, the saturation effect appeared as the pulse was ~4 ps ahead of the pump–probe process, and disappeared completely after ~1 ps behind. To validate the maximum inhibition, we investigated the saturated TA spectra dependent on the saturation laser power. As shown in Fig. 2(b), the normalized TA signal was suppressed significantly as the saturation power increased from 0 to 24 mW. The theoretical
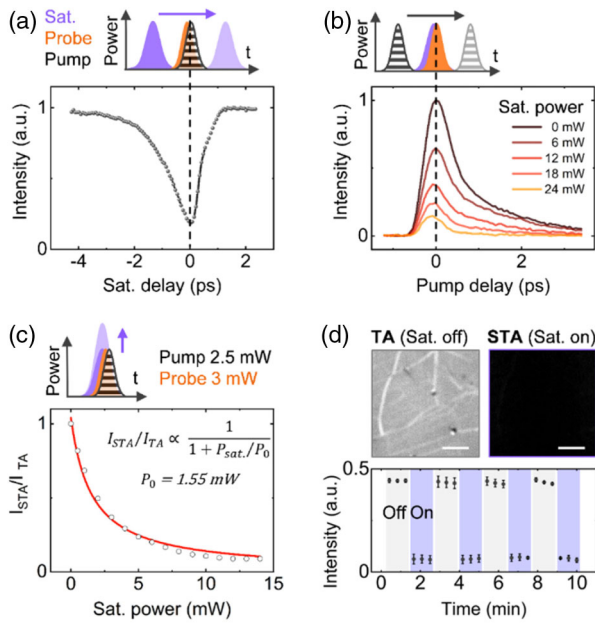
Fig. 2. Saturation characterization of TA process in graphene. (a) Suppression of TA signal at different delays of saturation pulse with respect to pump–probe pulse. (b) TA spectra attenuation at different saturation laser powers. (c) TA signal suppression as a function of the saturation power. The curve is fitted by Eq. (1). (d) TA, STA images and saturation-switching response of monolayer graphene. Scale bars, 5 μm.
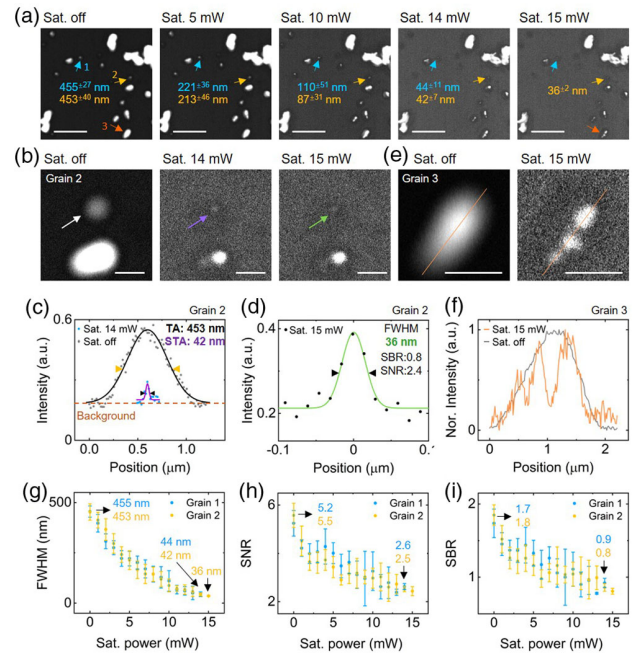

Fig. 3. Super-resolution imaging of nano-grains in graphene. (a) TA image shows diffraction-limited resolution of ∼453 nm, while STA images with increasing saturation power show improving resolution down to ∼36 nm. This is a more than 12-fold enhancement of resolution. Scale bars, 5 μm. (b) Zoom-in images of areas indicated by yellow arrows in (a). Scale bars, 1 μm. (c), (d) Cross-section profiles of the selected grain in (b). (e) Zoom-in images of areas indicated by orange arrows in (a). Scale bars, 1 μm. (f) Normalized intensity profiles along the lines in (e). (g)–(i) Measured FWHM, SNR, and SBR of grain 1 and grain 2 as a function of saturation laser power, respectively.

model of saturated absorption in graphene has been well studied and can be written as [22,29]

$$I_{STA}/I_{TA} \propto 1/(1 + P_{sat.}/P_0), \tag{1}$$

where I_{STA}/I_{TA} is the ratio of STA to TA signal, $P_{sat.}$ is the saturation laser power, and P_0 is the saturation laser power as the TA signal drops to half. In Fig. 2(c), we depict the dependence of the I_{STA}/I_{TA} on the saturation power. By fitting the data via Eq. (1), we obtained the value of P_0 to be 1.55 mW under the condition of a 2.5 mW pump laser and 3 mW probe laser. P_0 is about half the power of the excitation laser, which is much smaller than that in the NIR-STA system [22]. As the saturation power was increased to 14 mW, the saturation efficiency gradually reached ∼92%. Figure 2(d) illustrates the saturation-switching response of monolayer graphene. The TA signal always retrieved ∼100% as the 6 mW saturation laser was repeatedly applied on the graphene for 10 min during imaging. The saturation laser power increasing to 17 mW was also tested in Fig. S5, Supplement 1, and the results indicate that STAN possesses a high photo-damage threshold. In addition, both the STA and TA signals are proportional to the probe and pump lasers (Fig. S6, Supplement 1). But the saturation efficiency will decrease significantly with the TA signal. Thus, the relative weak laser power of about 2–3 mW is chosen for both pump and probe lasers in further super-resolution STA imaging.

Figure 3(a) presents the super-resolution STA images of nano-grains in graphene with gradually increased saturation laser power. Here, the laser powers of both pump and probe beams were fixed at 3 mW. In the absence of the donut-shaped saturation laser, the sizes of indicated nano-grains (arrows in blue and yellow) were measured to be 455 ± 27 nm and 453 ± 40 nm, respectively, which were defined by full width at half maximum (FWHM). As the saturation laser power was gradually increased to 14 mW,

we found that the measured sizes of the same grains reduced to 44 ± 11 nm and 42 ± 7 nm [zoom-in images in Fig. 3(b)], respectively, and also the TA signals decreased three to five folds. A direct comparison of the intensity profiles is presented in Fig. 3(c). The complete dataset is shown in Fig. S7, Supplement 1. Significantly, the spatial resolution of STA imaging improved to 36 nm when the saturation power was further increased to 15 mW [zoom-in image in Fig. 3(b) and intensity profile in Fig. 3(d)]. At this point, the grain in the image was still distinguishable, but the signal-to-background ratio (SBR) and signal-to-noise ratio (SNR) of this grain decreased to 0.8 and 2.4, respectively. In a direct comparison shown in Figs. 3(e) and 3(f), the STA image exhibits a substantially higher spatial resolution, where we can visualize three individual grains placed side by side rather than one larger elliptical spot appearing in the corresponding TA image. It is worth noting that the enhanced resolution compared with previous work [22,23] is due to the combination of effects of more efficient saturation and reduced saturation laser wavelength. Figure 3(g) shows that the measured grain width decreased gradually with the applied saturation laser power. The repeated experiments and results are shown in Fig. S8, Supplement 1. We also analyze both SNR and SBR of the measured grain signals in Figs. 3(h)–3(i). In the absence of the saturation laser, the widths of grains were measured to be ∼450 nm with SBR and SNR of their intensity profiles about 1.8 and 5.5, respectively. As 14 mW saturation laser was applied for super-resolution imaging, the measured width of grains were reduced to ∼42 nm with SBR of ∼0.8 and SNR of ∼2.5, in which the signals were just above the noise and background. The definition of
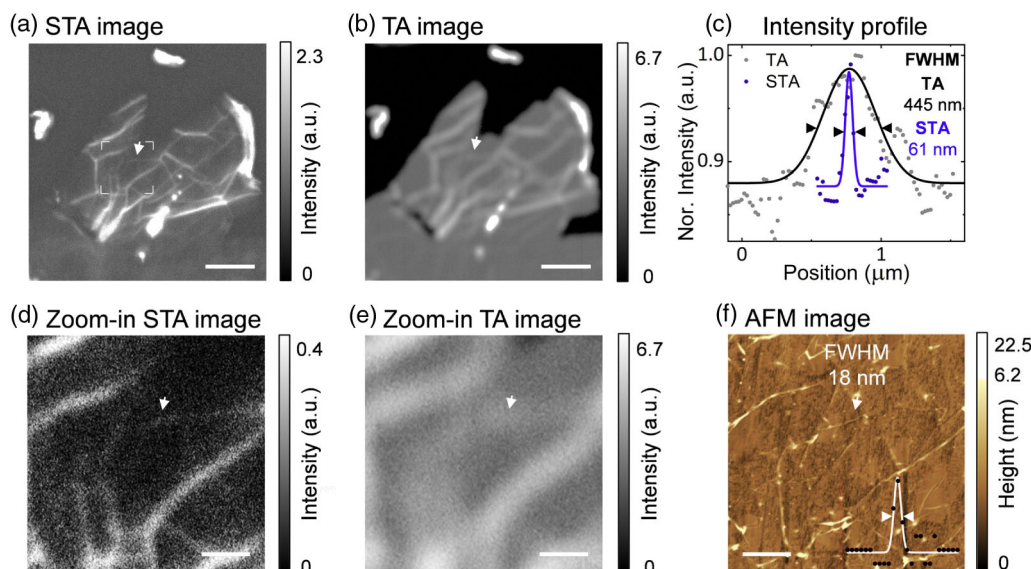
Fig. 4. Super-resolution imaging of nano-wrinkles in graphene. (a), (b) STA and TA images of monolayer graphene demonstrate the much higher resolution of the STA method. (c) Measured intensity profiles of the selected nano-wrinkles in (a) and (b), indicated by white arrows. Scale bars, 5 μm. (d), (e) Zoom-in STA (d) and TA (e) images corresponding to boxed regions in (a) and (b). (f) AFM image of the same areas as (d) and (e). Inset: cross-sectional height profile of the same nano-wrinkle indicated by the arrow. Scale bars, 1 μm.

the error bars is described in detail in the Experimental Section of Supplement 1. Thus, the further improvement of imaging resolution can be achieved by reducing TA noise or promoting detection sensitivity of the instrumentation. Meanwhile, the higher saturation laser power may not improve the resolution due to further suppression of TA signal. In addition, the potential photodamage caused by higher laser power is another major constraint for better spatial resolution.

With enhanced spatial resolution, we demonstrated super-resolution STA imaging of nano-wrinkles in monolayer graphene. Here, the graphene film was fabricated on a coverslip through a commonly used wet transfer method (see details in Experimental Section, Supplement 1). The non-uniform strain in the wrinkled region induces a modulated Dirac cone band structure [30,31] and funnel effect [32], and the photogenerated carriers migrate towards the center of the wrinkles, leading to enhanced carrier density, which contributes to the stronger TA signal in the wrinkled region compared with that of flat graphene. As shown in Figs. 4(a) and 4(b), the TA imaging and corresponding super-resolution STA imaging were performed in the same region of the graphene. As a direct comparison, the STA image exhibits a significantly improved spatial resolution and image contrast. To prove the resolution enhancement, we plot and compare the intensity profiles of a nano-wrinkle, indicated by arrows in Figs. 4(a) and 4(b). The Gaussian fitted FWHM of the nano-wrinkle was found to be 445 nm in the TA image and 61 nm in the super-resolution STA image [Fig. 4(c)]. Since the background is due to monolayer graphene, the intensity profile of STA presents SBR similar to TA, but much lower signal intensity (about three times attenuation). Here, the powers of pump, probe, and saturation lasers were set to be 2.5 mW, 2.5 mW, and 6 mW, respectively. Further in the boxed zoom-in region of Fig. 4(a), we directly compare STA and TA images [Figs. 4(d) and 4(e)] with the corresponding AFM image [Fig. 4(f)]. As a result, AFM confirmed that the investigated feature was a nano-wrinkle with FWHM of 18 nm and height of ~6 nm (Fig. S9, Supplement 1). Since the measured width of the

nano-wrinkle can be interpreted as the convolution of the effective point spread function (PSF) of the imaging system and the actual size of the sample, the resolution of our super-resolution STA nanoscope is calculated to be ~58 nm. Except for nano-wrinkles, graphene defects including grain boundaries, holes, multilayers, and edges can also be imaged with fine details by a super-resolution STA nanoscope (Fig. S10, Supplement 1). Thus, we proved that the proposed STA imaging method can significantly improve the spatial resolution in contrast to conventional TA microscopy.

In principle, the STAN can be applied to any 2D materials with a saturation effect. For different materials, one can experimentally tune the photon energy of the saturation laser according to the different bandgaps and achieve the most efficient saturation. To validate it, we further explored other 2D materials, including molybdenum ditelluride ($MoTe_2$) and black phosphorus (BP). $MoTe_2$, as a promising nonzero bandgap 2D material, also exhibits efficient saturation suppression and high photostability and is well suited for super-resolution imaging by the STAN system [Fig. S11(a), Supplement 1, including TA, STA images, and measurements of saturation response to fast switching lasers]. We also checked the performance of BP. Although BP is a type of saturable material and applicable to the STAN system, it is not very stable under laser excitation, possibly due to photo-oxidation at ambient conditions [33], and suffers from photodamage with a threshold of < 2 mW [Fig. S11(b), Supplement 1]. To alleviate the photodamage introduced to this type of sample, one could experimentally control the gas environment and broaden the pulse width of the saturation laser to reduce the peak power.

3. CONCLUSION

In conclusion, we have demonstrated a super-resolution far-field optical nanoscopy with spatial resolution of 36 nm for the first time. By using a short wavelength and donut-shaped saturation laser, the photons with higher energy can effectively terminate the TA process driven by NIR pump and probe lasers, and hence allow

about three-fold enhancement in spatial resolution compared with the previous record of ∼100 nm. To verify the actual spatial resolution achieved, we performed STA imaging of nano-grains and nano-wrinkles in monolayer graphene. We confirmed that the imaging resolution of the proposed method can reach 36 nm with ample SNR of 2.4 and SBR of about 0.8. For further study, we believe better spatial resolution can be achieved by enhancing detection sensitivity or shorter wavelength of TA lasers, instead of elevating the laser powers. The higher pump–probe laser power can promote TA signal sufficiently, but the saturation efficiency is bound to decline. On the other hand, the increased saturation laser power is beneficial to improve the spatial resolution, but the TA signal will be suppressed significantly as well. All in all, the developed far-field super-resolution STAN is well suited for fast morphological and electrical characterization of 2D materials with significantly reduced requirements for sample preparation and imaging environment. We envision that this optical nanoscope will be partially substituted for AFM, SEM, and NSOM for high-resolution imaging and identification of nanostructures in material science and applications.

Disclosures. The authors declare no conflicts of interest.

See Supplement 1 for supporting content.

†These authors contributed equally to this paper.

REFERENCES

1. S. J. Sahl, S. W. Hell, and S. Jakobs, "Fluorescence nanoscopy in cell biology," Nat. Rev. Mol. Cell Biol. **18**, 685–701 (2017).
2. B. Huang, H. Babcock, and X. Zhuang, "Breaking the diffraction barrier: super-resolution imaging of cells," Cell **143**, 1047–1058 (2010).
3. J. W. Lichtman and J.-A. Conchello, "Fluorescence microscopy," Nat. Methods **2**, 910–919 (2005).
4. Z. Fei, A. Rodin, G. O. Andreev, W. Bao, A. McLeod, M. Wagner, L. Zhang, Z. Zhao, M. Thiemens, and G. Dominguez, "Gate-tuning of graphene plasmons revealed by infrared nano-imaging," Nature **487**, 82–85 (2012).
5. J. Zhou, A. I. Chizhik, S. Chu, and D. Jin, "Single-particle spectroscopy for functional nanomaterials," Nature **579**, 41–50 (2020).
6. S. Chong, M. Wei, and X. S. Xie, "Ground-state depletion microscopy: detection sensitivity of single-molecule optical absorption at room temperature," J. Phys. Chem. Lett. **1**, 3316–3322 (2010).
7. J. Jahng, J. Brocious, D. A. Fishman, S. Yampolsky, D. Nowak, F. Huang, V. A. Apkarian, H. K. Wickramasinghe, and E. O. Potma, "Ultrafast pump-probe force microscopy with nanoscale resolution," Appl. Phys. Lett. **106**, 083113 (2015).
8. M. C. Fischer, J. W. Wilson, F. E. Robles, and W. S. Warren, "Invited review article: pump-probe microscopy," Rev. Sci. Instrum. **87**, 031101 (2016).
9. W. R. Silva, C. T. Graefe, and R. R. Frontiera, "Toward label-free super-resolution microscopy," ACS Photon. **3**, 79–86 (2016).
10. L. Wan, N. Yang, C. Y. Hiew, A. Schelleman, L. Johnson, C. May, and R. Bellomo, "An assessment of the accuracy of renal blood flow estimation by Doppler ultrasound," Intensive Care Med. **34**, 1503–1510 (2008).
11. Y. Bi, C. Yang, Y. Chen, S. Yan, G. Yang, Y. Wu, G. Zhang, and P. Wang, "Near-resonance enhanced label-free stimulated Raman scattering microscopy with spatial resolution near 130 nm," Light Sci. Appl. **7**, 81 (2018).
12. C. Krafft, M. Schmitt, I. W. Schie, D. Cialla-May, C. Matthäus, T. Bocklitz, and J. Popp, "Label-free molecular imaging of biological cells and tissues by linear and nonlinear Raman spectroscopic approaches," Angew. Chem. (Int. Ed.) **56**, 4392–4430 (2017).
13. D. Wang, S. Liu, Y. Chen, J. Song, W. Liu, M. Xiong, G. Wang, X. Peng, and J. Qu, "Breaking the diffraction barrier using coherent anti-Stokes Raman scattering difference microscopy," Opt. Express **25**, 10276–10286 (2017).
14. J. Ling, X. Miao, Y. Sun, Y. Feng, L. Zhang, Z. Sun, and M. Ji, "Vibrational imaging and quantification of two-dimensional hexagonal boron nitride with stimulated Raman scattering," ACS nano **13**, 14033–14040 (2019).
15. C. Silien, N. Liu, N. Hendaoui, S. A. M. Tofail, and A. Peremans, "A framework for far-field infrared absorption microscopy beyond the diffraction limit," Opt. Express **20**, 29694–29704 (2012).
16. D. Joshi, M. Hauser, G. Veber, A. Berl, K. Xu, and F. R. Fischer, "Super-resolution imaging of clickable graphene nanoribbons decorated with fluorescent dyes," J. Am. Chem. Soc. **140**, 9574–9580 (2018).
17. K. Zhanghao, L. Chen, X.-S. Yang, M.-Y. Wang, Z.-L. Jing, H.-B. Han, M. Q. Zhang, D. Jin, J.-T. Gao, and P. Xi, "Super-resolution dipole orientation mapping via polarization demodulation," Light Sci. Appl. **5**, e16166 (2016).
18. V. Scutelnic, A. Prlj, A. Zabuga, C. Corminboeuf, and T. R. Rizzo, "Infrared spectroscopy as a probe of electronic energy transfer," J. Phys. Chem. Lett. **9**, 3217–3223 (2018).
19. L. Gong, W. Zheng, Y. Ma, and Z. Huang, "Higher-order coherent anti-Stokes Raman scattering microscopy realizes label-free super-resolution vibrational imaging," Nat. Photonics **14**, 115–122 (2019).
20. G. Xing, H. Guo, X. Zhang, T. C. Sum, and C. H. A. Huan, "The physics of ultrafast saturable absorption in graphene," Opt. Express **18**, 4564–4573 (2010).
21. A. Marini, J. Cox, and F. G. De Abajo, "Theory of graphene saturable absorption," Phys. Rev. B **95**, 125408 (2017).
22. P. Wang, M. N. Slipchenko, J. Mitchell, C. Yang, E. O. Potma, X. Xu, and J. X. Cheng, "Far-field imaging of non-fluorescent species with sub-diffraction resolution," Nat. Photonics **7**, 449–453 (2013).
23. G. Zanini, K. Korobchevskaya, T. Deguchi, A. Diaspro, and P. Bianchini, "Label-free optical nanoscopy of single-layer graphene," ACS Nano **13**, 9673–9681 (2019).
24. W. Bao, M. Melli, N. Caselli, F. Riboli, D. Wiersma, M. Staffaroni, H. Choo, D. Ogletree, S. Aloni, and J. Bokor, "Mapping local charge recombination heterogeneity by multidimensional nanospectroscopic imaging," Science **338**, 1317–1321 (2012).
25. A. Martinez and Z. P. Sun, "Nanotube and graphene saturable absorbers for fibre lasers," Nat. Photonics **7**, 842–845 (2013).
26. Q. L. Bao, H. Zhang, Y. Wang, Z. H. Ni, Y. L. Yan, Z. X. Shen, K. P. Loh, and D. Y. Tang, "Atomic-layer graphene as a saturable absorber for ultrafast pulsed lasers," Adv. Funct. Mater. **19**, 3077–3083 (2009).

27. Z. Sun, T. Hasan, F. Torrisi, D. Popa, G. Privitera, F. Wang, F. Bonaccorso, D. M. Basko, and A. C. Ferrari, "Graphene mode-locked ultrafast laser," ACS Nano **4**, 803–810 (2010).

28. J. W. You, S. R. Bongu, Q. Bao, and N. C. Panoiu, "Nonlinear optical properties and applications of 2D materials: theoretical and experimental aspects," Nanophotonics **8**, 63–97 (2019).

29. F. T. Vasko, "Saturation of interband absorption in graphene," Phys. Rev. B **82**, 245422 (2010).

30. N. Levy, S. A. Burke, K. L. Meaker, M. Panlasigui, A. Zettl, F. Guinea, A. H. C. Neto, and M. F. Crommie, "Strain-induced pseudo-magnetic fields greater than 300 Tesla in graphene nanobubbles," Science **329**, 544–547 (2010).

31. D. Edelberg, H. Kumar, V. Shenoy, H. Ochoa, and A. N. Pasupathy, "Tunable strain soliton networks confine electrons in Van Der Waals materials," Nat. Phys. (2020), https://doi.org/10.1038/s41567-020-0953-2.

32. J. Feng, X. F. Qian, C. W. Huang, and J. Li, "Strain-engineered artificial atom as a broad-spectrum solar energy funnel," Nat. Photonics **6**, 866–871 (2012).

33. T. Ahmed, S. Balendhran, M. N. Karim, E. L. H. Mayes, M. R. Field, R. Ramanathan, M. Singh, V. Bansal, S. Sriram, M. Bhaskaran, and S. Walia, "Degradation of black phosphorus is contingent on UV–blue light exposure," npj 2D Mater. Appl. **1**, 18 (2017).